

# VORTEX-PATTERNS OF A 2D ROTATING BOSE-EINSTEIN CONDENSATE AT THE CRITICAL ROTATIONAL SPEED

BAO-DUY LE\*

Faculty of Physics and Engineering Physics,  
University of Science, Ho Chi Minh City, Vietnam.  
and

Vietnam National University, Ho Chi Minh City, Vietnam.

DINH-THI NGUYEN†

Faculty of Mathematics and Computer Science,  
University of Science, Ho Chi Minh City, Vietnam.  
and

Vietnam National University, Ho Chi Minh City, Vietnam.

(Dated: November 18, 2025)

We introduce a GPU-accelerated variational framework with exact projection onto the Lowest Landau Level to probe vortex patterns in rapidly rotating two-dimensional Bose-Einstein condensates. For repulsive interactions, our approach faithfully reproduces Abrikosov vortex lattices, achieving quantitative alignment with Thomas-Fermi theory and the Abrikosov constant, while underscoring the profound analogy between superfluid vortex ordering and Abrikosov lattices in type-II superconductors. In the attractive regime, we reveal that weak attractions sustain stable vortex arrays, whereas stronger attractions quench vortices, trigger radial contraction, and culminate in collapse at the Gagliardo-Nirenberg threshold. These findings deliver a cohesive numerical benchmark for vortex formation and collapse dynamics, forging a rigorous link between superfluidity and superconductivity in rotating quantum matter.

**Keywords:** Bose-Einstein condensates; fast rotation; Lowest Landau Level; Abrikosov vortex lattice; superfluidity-superconductivity correspondence; attractive interactions and collapse; Gross-Pitaevskii equation.

## I. INTRODUCTION

Since the groundbreaking experimental realization of Bose-Einstein condensation (BEC) in dilute alkali vapors in 1995 [1], the study of ultra-cold quantum many-body systems has undergone a remarkable evolution. A BEC forms when a significant fraction of bosons coherently occupies the lowest quantum state, giving rise to striking phenomena such as superfluidity, the formation of quantized vortices, and macroscopic quantum coherence. While early theoretical models focused on non-interacting Bose gases, subsequent research has illuminated the pivotal role of inter-particle interactions in shaping the condensate's properties, dynamics, and stability [2].

### A. Many-body Hamiltonian

The many-body Hamiltonian provides the foundational framework for describing interacting bosonic systems (in the units of Planck constant and particle mass,

i.e.,  $\hbar = m = 1$ ). For a system of  $N$  identical bosons confined in a two-dimensional harmonic trap rotating at angular frequency  $\Omega$ , the Hamiltonian is expressed as

$$H_N = \sum_{j=1}^N \left( -\frac{1}{2} \Delta_{x_j} - \Omega L_{z_j} + \frac{1}{2} |x_j|^2 \right) + \sum_{i < j} \kappa \delta_0(x_i - x_j). \quad (1)$$

Here  $L_{z_j}$  denotes the angular momentum operator, defined by  $L_{z_j} = -i x_j^\perp \cdot \nabla_{x_j}$ , with  $x_j \in \mathbb{R}^2$  the position of the  $j^{\text{th}}$  particle and  $z_j \in \mathbb{C}$  its associated complex coordinate. Furthermore,  $\kappa \in \mathbb{R}$  denotes the interaction strength, with positive values indicating repulsion and negative values attraction. The delta-function interaction approximates the short-range two-body potential typical of dilute gases [3].

### B. Interactions parameter

The sign of  $\kappa$  dictates the stability of rotating condensates. Repulsive interactions ( $\kappa > 0$ ) stabilize the system and give rise to quantized vortex lattices, analogous to Abrikosov patterns in superconductors [4]. Attractive interactions ( $\kappa < 0$ ), by contrast, lead to collapse beyond the sharp Gagliardo-Nirenberg (GN) threshold (18), where the blow-up profile is given by the unique pos-

\* Email: 24130012@student.hcmus.edu.vn

† Email: ndthi@hcmus.edu.vn

itive radial ground state [5]. In the rapid-rotation limit  $\Omega \nearrow 1$ , dynamics are confined to the Lowest Landau Level (LLL), yielding Thomas–Fermi–like (TF) vortex crystals for repulsive gases, while attractive gases display vortices only transiently before destabilization [6, 7].

We present a unified numerical framework that enforces exact projection onto the LLL. For  $\kappa > 0$ , constrained minimization of the GP functional within the LLL basis, accelerated by automatic differentiation on GPUs, reproduces the Abrikosov energy  $e^{\text{Ab}}(1)$  (8) with systematic convergence. For  $\kappa < 0$ , imaginary-time evolution with Strang splitting and spectral filtering captures both vortex formation at weak attraction and the GN-governed collapse at stronger coupling [8]. Together, these results offer a comprehensive numerical validation of two cornerstone regimes in rapidly rotating 2D BECs: vortex crystallization and critical blow-up.

## II. THEORETICAL FRAMEWORK

### A. Mean-field Approximation

Consider a system of  $N$  identical bosons in  $\mathbb{R}^2$ , confined by a harmonic potential and rotating with angular velocity  $\Omega \in [0, 1)$ . The associated quantum Hamiltonian in the rotating frame is defined in (1). In the mean-field limit:  $N \rightarrow \infty$  with fixed  $\kappa$ , it can be shown (see [3, 9]) that the system’s ground state exhibits complete BECs. That is, the many-body wavefunction concentrates on product states  $\Psi_N(x_1, \dots, x_N) \approx \prod_{j=1}^N \psi(x_j)$ , and the energy per particle converges to the nonlinear functional:

$$\mathcal{E}_{\Omega, G}^{\text{GP}}[\psi] = \int_{\mathbb{R}^2} \left[ \frac{1}{2} |(-i\nabla - \Omega x^\perp) \psi|^2 + \frac{G}{4} |\psi|^4 + \frac{1 - \Omega^2}{2} |x|^2 |\psi|^2 \right], \quad \|\psi\|_{L^2}^2 = 1. \quad (2)$$

The effective interaction strength is defined as  $G = 2\kappa N$ , representing the mean-field limit of the many-body interaction. The sign of  $G$  dictates the condensate behavior: repulsive for  $G > 0$  and attractive for  $G < 0$ .

In the rotating frame with angular velocity  $\Omega$ , the GP functional acquires the contribution  $-\Omega L_{z_j}$ . Completing the square in the kinetic and trapping terms yields

$$V_\Omega^{\text{eff}}(x) = \frac{(1 - \Omega^2)|x|^2}{2}, \quad (3)$$

this phenomenon captures the competition between harmonic confinement and centrifugal forces. As  $\Omega \nearrow 1$ , the trap weakens and the condensate enters the LLL, where dynamics resemble those of charged particles in a magnetic field [7, 10]. Repulsive gases then form ordered vortex lattices or giant-vortex states, whereas attractive gases lose stabilization and collapse. Thus, the balance of  $V_\Omega^{\text{eff}}$  and rotation governs the density profile, vortex geometry, and onset of instabilities.

### B. Lowest Landau Level regime

In the fast-rotation limit  $\Omega \nearrow 1$ , centrifugal and trapping terms nearly cancel, confining the condensate to the LLL [10]. Wave functions then take the analytic form

$$\psi(z) = f(z) e^{-\frac{\Omega|z|^2}{2}}, \quad z = x + iy, \quad (4)$$

where  $f(z)$  is an entire analytic (holomorphic) function. Moreover, we can define  $f(z)$  by an ansatz [11] for the LLL in the form:

$$\psi(z) = c \prod_{j=1}^J (z - z_j) e^{-\frac{\Omega|z|^2}{2}} \quad (5)$$

where  $c$  is a normalization constant  $L^2$  and  $z_1, \dots, z_J$  are the locations of the zeros of the analytical function associated with  $\psi$ . Vortices are encoded in the zeros of  $f$ , forming triangular lattices with infinitely many zeros, including “invisible” ones outside the TF region [12]. The projected LLL energy functional reads

$$\mathcal{E}_{\Omega, G}^{\text{LLL}}[\psi] = \Omega + \int_{\mathbb{R}^2} \left[ \frac{G}{4} |\psi|^4 + \frac{1 - \Omega^2}{2} |x|^2 |\psi|^2 \right]. \quad (6)$$

### C. Thomas–Fermi theory

In the repulsive regime of trapped dilute BECs, the TF approximation provides an accurate macroscopic density profile when kinetic energy is negligible [2]. Under rapid rotation, the condensate is confined to the LLL and the GP functional reduces to an effective TF form [4, 13]:

$$\mathcal{E}_{\Omega, G}^{\text{LLL}}[\psi] - \Omega \underset{\Omega \nearrow 1}{\approx} \mathcal{E}_{\Omega, G}^{\text{TF}}[\rho] := \int_{\mathbb{R}^2} \frac{e^{\text{Ab}}(1)G}{4} \rho^2 + \frac{1 - \Omega^2}{2} |x|^2 \rho. \quad (7)$$

The Abrikosov constant  $e^{\text{Ab}}(1)$  characterizes the minimal quartic interaction energy in the LLL [10], i.e.,

$$e^{\text{Ab}}(1) = \lim_{L \rightarrow \infty} \inf_{\substack{\psi \in \mathcal{LLL}_L \\ \|\psi\|_{L^2} = 1}} \int_{\mathbb{R}^2} |\psi(x)|^4 dx. \quad (8)$$

The TF density profile defined by [2, 14]

$$\rho_{\Omega=0, G=1}^{\text{TF}}(x) = [\mu - |x|^2]_+, \quad (9)$$

where  $\mu > 0$  is the chemical potential

$$\mu = \rho_{\Omega=0, G=1}^{\text{TF}} + |x|^2 \quad (10)$$

and  $[\cdot]_+$  denotes the positive part. As  $\Omega \nearrow 1$ , the wave function assumes the analytic form (4), and the corresponding energy functional reduces to (7). Within this regime, the condensate density is accurately captured by a TF profile:

$$\rho_{\Omega, G}^{\text{TF}}(x) = \frac{1 - \Omega^2}{e^{\text{Ab}}(1)G} (\lambda^{\text{TF}} - |x|^2)_+, \quad (11)$$

with  $\lambda^{\text{TF}} > 0$  fixed by normalization from (7)

$$\lambda^{\text{TF}} = e^{\text{Ab}}(1)G\rho_{\Omega,G}^{\text{TF}} + (1 - \Omega^2)|x|^2. \quad (12)$$

This profile captures the vortex-lattice structure and differs from the classical TF law (9) due to the analytic constraint of the LLL projection.

#### D. Cubic GP and blow-up for attractive interactions

For attractive interactions ( $G < 0$ ), the 2D condensate is governed at the mean-field level by the focusing cubic GP equation

$$i\partial_t\psi = [-\Delta + 2V_{\Omega=0}^{\text{eff}} + G|\psi|^2 - \Omega L_{z_j}] \psi, \quad (13)$$

with  $\psi \in H^1(\mathbb{R}^2) = \{\psi \in L^2(\mathbb{R}^2) \mid \nabla\psi \in L^2(\mathbb{R}^2)\}$ . In this regime, solutions may blow up in finite time, corresponding to macroscopic collapse [15–17]. Seeking stationary states  $\psi(x, t) = e^{-i\mu t}u(x)$  leads to the nonlinear elliptic problem

$$-\Delta u + 2V_{\Omega=0}^{\text{eff}}u + G|u|^2u = \mu u, \quad (14)$$

which admits radially symmetric solutions, with  $\mu$  is chemical potential. In the  $L^2$ -critical case, collapse profiles converge (after rescaling) to the unique positive ground state  $Q \in H^1(\mathbb{R}^2)$  solving

$$-\Delta Q + Q - Q^3 = 0, \quad (15)$$

with universal asymptotics

$$u(x) \sim \frac{1}{\lambda_G}Q\left(\frac{x}{\lambda_G}\right) \quad (16)$$

where  $\lambda_G \rightarrow 0$  is collapse length scale (see Section IV C). The ground state  $Q$  saturates the sharp GN inequality

$$\|u\|_{L^4}^4 \leq \frac{2}{\|Q\|_{L^2}^2} \|u\|_{L^2}^2 \|\nabla u\|_{L^2}^2, \quad (17)$$

and its  $L^2$  norm determines the collapse threshold

$$G_* = \|Q\|_{L^2}^2 = 2\pi \int_0^\infty Q(x)^2 x dx. \quad (18)$$

The dichotomy between global existence and blow-up is well understood (see [17–19]):

- **Stable regime ( $G > -G_*$ ):** There exist initial data  $\psi \in H^1 \cap L^2(|x|^2 dx)$  such that the solution blows up in finite time, i.e.  $\lim_{t \rightarrow T_{\max}} \|\psi\|_{H^1} = \infty$  for some  $T_{\max} < \infty$ .
- **Blow-up regime ( $G < -G_*$ ):** Equation (13) admits global solutions for all  $H^1$  initial data  $\psi_0$  with  $\|\psi_0\|_{L^2} = 1$ .

Near criticality  $G \searrow -G_*$ , the condensate is well approximated by rescaled  $Q$ , and rigorous results confirm that the GP model captures the many-body dynamics up to blow-up time [17].

### III. NUMERICAL METHODS AND RESULTS

#### A. Local density approximation

To investigate the ground state of a 2D BEC with  $G > 0$  under near-critical rotation ( $\Omega \nearrow 1$ ), we adopt a variational formulation restricted to the LLL. The condensate wave function is expanded in the orthonormal basis

$$\phi_k(z) = \frac{1}{\sqrt{\pi k!}} z^k e^{-|z|^2/2}, \quad k = 0, 1, \dots, N^{\text{basis}} - 1, \quad (19)$$

with  $z = x + iy$ , and the GP energy functional in the LLL subspace is minimized under the normalization constraint. The coefficients  $c_k$  are treated as complex variational parameters, optimized by constrained minimization [20, 21]. An initial guess containing a hexagonal ring of vortices is projected onto the LLL, ensuring efficient convergence to vortex-lattice states.

The resulting minimizers exhibit the characteristic features of rapidly rotating condensates. The macroscopic profile follows the TF envelope, while the microscopic structure reveals a triangular Abrikosov vortex lattice [22, 23]. Close to the trap center, the lattice is nearly perfect, whereas mild distortions appear near the boundary due to finite-size effects. The computed vortex density and interaction energy are consistent with the Abrikosov parameter  $e^{\text{Ab}}(1)$  [4], confirming that the LLL variational framework accurately captures the interplay between rotation, interactions, and vortex formation.

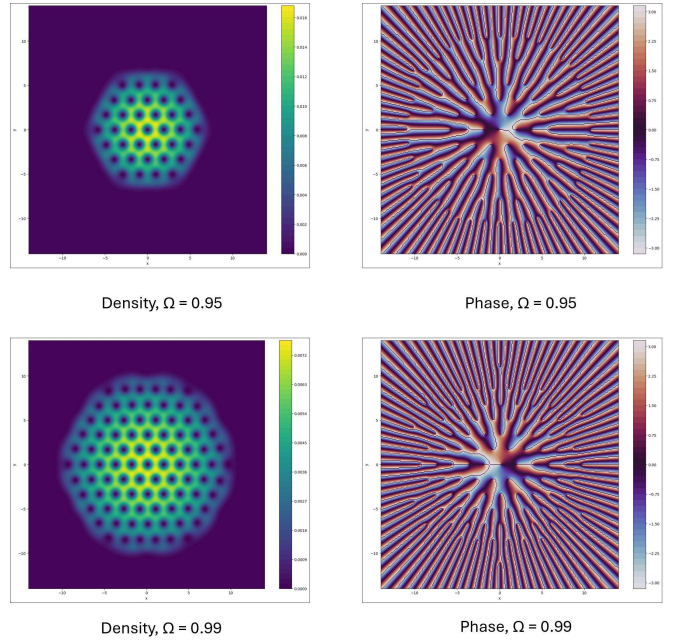


FIG. 1: Density and phase of the condensate wave function  $|\psi_\Omega|^2$  for  $G = 200$  in the weak effective trap  $V_\Omega^{\text{eff}}$  [see (3)]. Results are shown for rotation frequencies  $\Omega = 0.95$  and  $\Omega = 0.99$ .

Figure 1 illustrates the formation of a vortex lattice closely resembling the Abrikosov structure observed in experiments [23]. The corresponding GP energy functional in the LLL is expressed in (6), proportional to  $G$ , accounting for the interaction energy. As  $\Omega$  increases, the interaction contribution becomes dominant, resulting in a flatter density distribution and a higher vortex density, consistent with energy minimization under the normalization constraint and its connection to the Abrikosov problem [4].

Then, we analyze the system at fixed rotational frequency while gradually increasing the repulsive interaction strength. In Figure 2, for weak interactions, only a few vortices appear near the center, resulting in a sparse configuration. At intermediate coupling, the vortex array expands radially and develops into a nearly triangular Abrikosov lattice. For sufficiently strong interactions, the condensate radius grows markedly, and the vortex density converges to the Abrikosov constant, in excellent agreement with the TF–LLL prediction [4].

The monotonic increase in vortex number with interaction strength underscores the dual role of repulsion: it suppresses density fluctuations while simultaneously driving spatial expansion, thereby facilitating vortex nucleation. Physically, stronger interactions render the condensate more incompressible, enabling it to accommodate a larger vortex lattice before energy minimization favors giant-vortex states or fragmentation at ultra-high, further reinforcing the analogy between rotating BECs and superconducting systems [24–26].

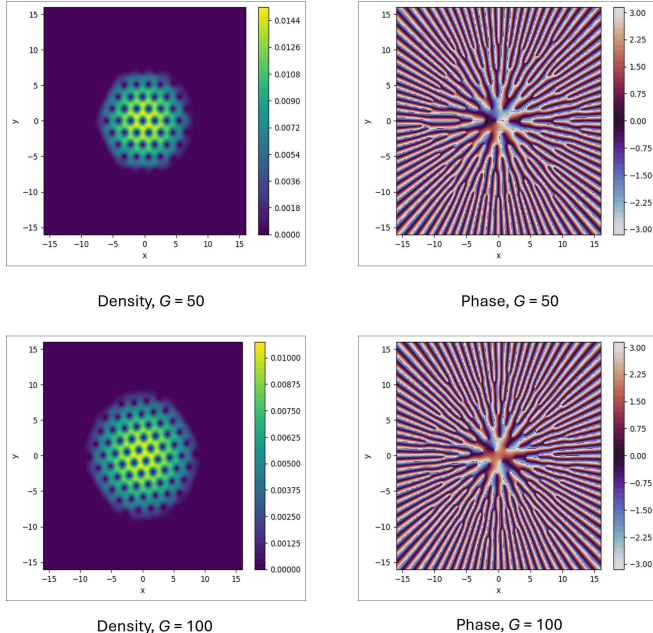


FIG. 2: Density of the condensate wave function  $|\psi_G|^2$  for repulsive interactions in the weak effective trap  $V_{\Omega=0.99}^{\text{eff}}$  [see (3)]. The vortex pattern and corresponding energy distributions are shown for interaction strengths  $G = 50$  and  $G = 100$ .

We now specialize the TF–LLL functional, corresponding to a rotation harmonic trap  $V_{\Omega}^{\text{eff}}(x)$ . The TF energy associated to the effective TF functional (7) with the minimizer has the inverted parabolic form (11), supported in the disk  $R^{\text{TF}} = \sqrt{\lambda^{\text{TF}}}$ . Imposing  $\int_{\mathbb{R}^2} \rho_{\Omega,G}^{\text{TF}} = 1$ , it yields

$$1 = 2\pi \int_0^{R^{\text{TF}}} \rho_{\Omega,G}^{\text{TF}}(r) r dr = \frac{\pi(1 - \Omega^2)}{e^{\text{Ab}}(1)G} \cdot \frac{(\lambda^{\text{TF}})^2}{2},$$

Then, by substituting (11) into (7) and integrating explicitly. The Abrikosov constant can be expressed directly in terms of the minimal TF energy as

$$e^{\text{Ab}}(1) = \frac{9\pi}{2G(1 - \Omega^2)} (\mathcal{E}_{\Omega,G}^{\text{TF}} [\rho_{\Omega,G}^{\text{TF}}])^2. \quad (20)$$

The number of vortices is quantified by computing the curl of the phase gradient of the optimized wavefunction,

$$\text{curl}\theta = \partial_x \theta_y - \partial_y \theta_x, \quad (21)$$

where  $\theta_x$  and  $\theta_y$  are approximated using finite differences. Vortices are identified at points  $|\text{curl}\theta| \approx 2\pi$ . The average density per vortex is calculated as:

$$e^{\text{sim}} = \frac{\|\psi\|_{L^2}^2}{N_v^{\text{sim}} \cdot c_n} \quad (22)$$

where  $N_v^{\text{sim}}$  is the number of detected vortices and  $c_n$  is the numerical parameter. This is compared to the theoretical Abrikosov parameter  $e^{\text{Ab}}(1) \approx 1.1596$  [22].

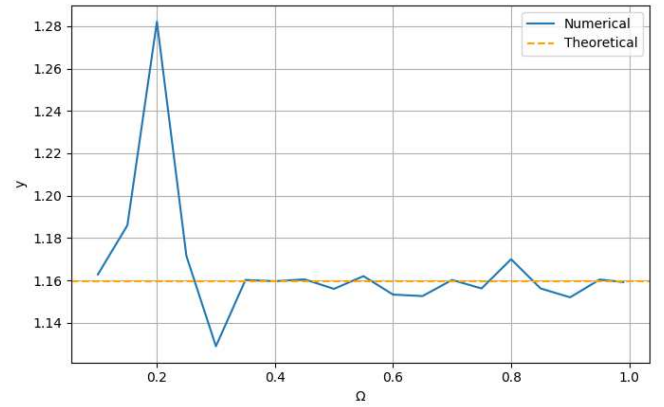


FIG. 3: Determine the theoretical energy density  $e^{\text{Ab}}(1)$  with  $G = 200$  in different  $\Omega$  rotation levels in LLL space via the numerical mean-field, with the weak interaction potential  $V_{\Omega}^{\text{eff}}$  in (3).

In the TF–LLL regime, simulations yield an average density per vortex,  $e^{\text{sim}}$ , that remains in excellent agreement with  $e^{\text{Ab}}(1)$  across all tested values of  $\Omega$  (see Figure 3). This consistency demonstrates the robustness of the vortex lattice in the LLL against variations in interaction strength, a direct consequence of the highly degenerate energy landscape imposed by the LLL constraint. At

large  $\Omega$ , the interaction term dominates, leading to a flattened density profile and stabilization of the hexagonal Abrikosov lattice. At smaller  $\Omega$ , quantum fluctuations produce slight deviations; nevertheless, the close agreement between  $e^{\text{sim}}$  and  $e^{\text{Ab}}(1)$  underscores the persistence of the TF description throughout the LLL regime.

In order to enable a meaningful comparison with the condensate number density, we smooth out the rapid oscillations induced by the vortex lattice and contrast the rotationally averaged profile with the theoretical TF prediction (Figure 4). The agreement is excellent, particularly regarding the TF radius, and the root-mean-square (RMS) error [27]:

$$\text{RMS} = \sqrt{\frac{1}{N} \sum_{i=1}^N [\rho^{\text{sim}}(x_i) - \rho^{\text{TF}}(x_i)]^2}, \quad (23)$$

Across a broad range of rotation frequencies  $\Omega$ , the RMS error remains consistently small at  $\mathcal{O}(10^{-3})$  (see Table VI), demonstrating that the optimized vortex-lattice solutions accurately reproduce the theoretical TF profile even in the strongly nonlinear regime. This agreement validates both the accuracy and robustness of the LLL implementation for rapidly rotating repulsive condensates. In addition, the optimization procedure exhibits high computational efficiency, which reports the iteration count, function evaluations, optimality, RMS error, and execution time for different  $\Omega$ . The nearly constant RMS across all cases highlights the stability of the algorithm, while the moderate computational cost confirms its suitability for large-scale parameter explorations.

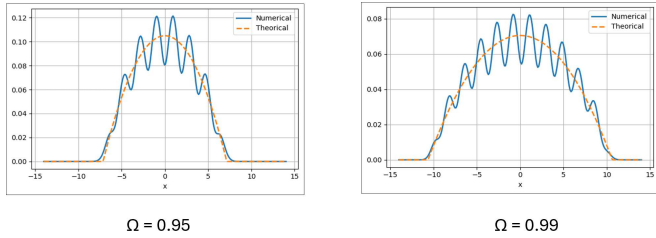


FIG. 4: Theoretical (red) and numerical (blue) density for mean-field approximation distribution, with  $G = 200$  (repulsive interaction), for  $\Omega = 0.95, 0.99$ .

## B. Collapse in mean-field limit

For attractive interactions ( $G < 0$ ) confined in a harmonic trap and subject to rapid rotation. The condensate wavefunction  $\psi(x, t) \in \mathbb{C}$  evolves according to the GP equation (13), where  $V_{\Omega}^{\text{eff}}(x)$  denotes the external confinement given by (3) and

$$L_{z_j} = -i(x\partial_y - y\partial_x)$$

The normalization

$$\int_{\mathbb{R}^2} |\psi(x, t)|^2 dx = 1 \quad (24)$$

is enforced at every step to ensure conservation of the total particle number. Then, we perform imaginary-time propagation  $t \mapsto -i\tau$ , which transforms the GPE into the nonlinear diffusion-type equation

$$\partial_{\tau} \psi = \Delta \psi - 2V_{\Omega=0}^{\text{eff}} \psi - G|\psi|^2 \psi + \Omega L_{z_j} \psi, \quad (25)$$

subject to the constraint (24). This equation is integrated using a time-splitting spectral scheme. The kinetic term is treated exactly in Fourier space, where each mode evolves as

$$\hat{\psi}(k) \mapsto \hat{\psi}(k) \exp\left(-\frac{1}{2}|k|^2 \Delta \tau\right),$$

while the potential and nonlinear contributions are updated explicitly in real space.

The computational domain is the square  $[-L, L]^2$  discretized uniformly on an  $N \times N$  grid. All quantities are expressed in trap units. A typical imaginary-time step satisfies  $\Delta\tau \sim 10^{-3}\text{--}10^{-2}$ , which provides both numerical stability and rapid convergence for the relaxation flow used to obtain the nonrotating ground state.

We employ imaginary-time propagation of the GPE equation (25) which monotonically decreases the energy functional:

$$\mathcal{E}_{\Omega=0, G}^{\text{GP}}[\psi] = \frac{1}{2} \int_{\mathbb{R}^2} |\nabla \psi|^2 + \int_{\mathbb{R}^2} V_{\Omega=0}^{\text{eff}} |\psi|^2 + \frac{G}{4} \int_{\mathbb{R}^2} |\psi|^4. \quad (26)$$

After each time step the wave function is renormalized,

$$\int_{[-L, L]^2} |\psi|^2 dx = 1, \quad (27)$$

to control collapse instabilities in the attractive regime near the critical coupling  $G_*$ .

To break radial symmetry and accelerate vortex nucleation we initialize the flow with a Gaussian envelope,

$$\psi_0(x) = Ae^{-\frac{1-\Omega^2}{2}x^2} \quad (28)$$

with  $A$  is an explicit vortex ansatz. Imprinting phase singularities raises the total kinetic energy through the flow term [14, 28]:

$$E^{\text{flow}} = \frac{1}{2} \int_{\mathbb{R}^2} \rho |\nabla S|^2 dx, \quad (29)$$

represents the kinetic energy of the superfluid current associated with the phase gradient  $\mathbf{v} = \nabla S$ . The kinetic cost  $E^{\text{flow}}$  to the background (nonrotating) energy, so that the total energy in the laboratory frame becomes

$$E^{\text{img}} = \mathcal{E}_{\Omega=0, G}^{\text{GP}}[\psi] + E^{\text{flow}}. \quad (30)$$

Once the nonrotating ground state is obtained, dynamics including the rotational term are evolved in real time according to the rotating-frame GPE (13). The rotation term  $-\Omega L_z$  is incorporated as a separate operator within the Strang-splitting scheme [21]. Its action corresponds to a rigid rotation of the condensate by an angle  $\theta = \Omega\Delta\tau$ , realized through the affine transformation

$$\psi_\theta(x) = \psi(R_{-\theta}x), \quad R_{-\theta} = \begin{pmatrix} \cos \theta & \sin \theta \\ -\sin \theta & \cos \theta \end{pmatrix},$$

which is implemented numerically via bilinear interpolation to maintain continuity and suppress spurious boundary effects. In the rotating frame, the relevant functional reads

$$\mathcal{E}_{\Omega, G, \theta}^{\text{GP}}[\psi] = E^{\text{img}} - \Omega \int_{\mathbb{R}^2} \psi_\theta L_z \psi_\theta, \quad (31)$$

and vortex configurations minimize  $\mathcal{E}_{\Omega, G, \theta}^{\text{GP}}$  by converting angular momentum into quantized circulation. In this weakly attractive regime, the condensate remains sufficiently extended so that the rigid-body (Feynman) estimate for the vortex surface density is approximately realized, and consequently, a regular vortex lattice is energetically favored [14].

When the attraction strength increases, the nonlinear term drives radial contraction of the condensate, leading to density accumulation at the center. At fixed rotation frequency, the vortex number  $N_v^{\text{sim}}$  is set by the product of the vortex surface density and the condensate area; hence a smaller radius directly implies fewer vortices. From an energetic perspective, stronger attraction disfavors the maintenance of extended low-density vortex cores, making states with reduced  $N_v^{\text{sim}}$  and enhanced central density more favorable. This mechanism is clearly reflected in the simulations: the vortex lattice becomes progressively sparser, the central density rises  $\langle x^2 \rangle$ , and the mean-square radius decreases, where

$$\langle x^2 \rangle := \int_{\mathbb{R}^2} |x|^2 |\psi(x)|^2 dx. \quad (32)$$

As  $G \searrow -G_*$ , the attractive interaction dominates over both quantum pressure and trapping, ultimately driving the condensate to collapse. In simulations, this regime manifests as a rapid growth of the peak density  $|\psi(r)|_{\text{max}}^2$ , a strong negative shift of the interaction energy, and a marked reduction of  $\langle x^2 \rangle$ , culminating in numerical breakdown. Figure 5 are in full agreement with theoretical predictions for 2D attractive condensates governed by the GPEs [29–31].

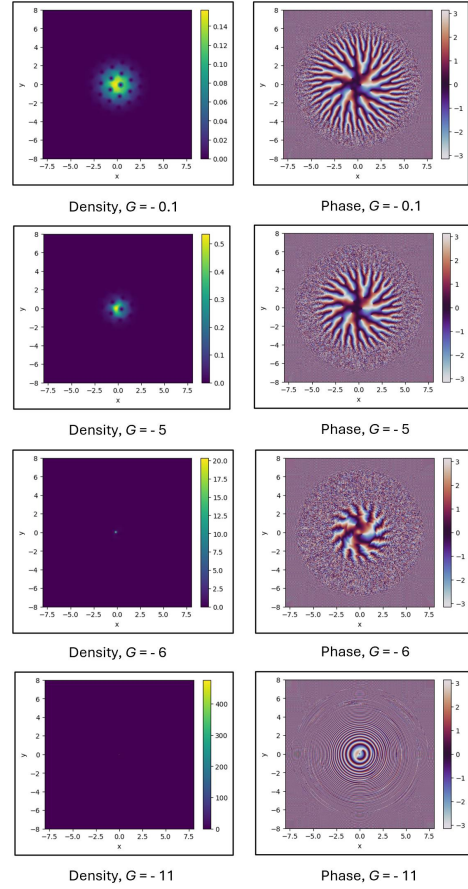


FIG. 5: Density and phase profiles of the condensate with attractive interactions at  $\Omega = 0.9$  for different  $G$ , obtained after  $10^4$  imaginary-time steps and  $2 \times 10^3$  real-time steps toward the energy-optimal ground state.

In Figure 6 moderate rotation ( $\Omega = 0.7$ ) the density remains centrally localized with few visible cores, consistent with collapse tendency. At higher rotation ( $\Omega = 0.99$ ), distinct vortex cores emerge in both density and phase, showing that centrifugal effects can overcome weak attraction. The qualitative trend mirrors the repulsive case: vortex number increases with angular velocity and begins to exhibit lattice ordering [11, 21, 32].

Identical vortex seeds were used across scans, so the reduction in vortex number with increasing  $|G|$  reflects genuine energetic shifts. Attractive cases were obtained by full GPE evolution, in contrast to the LLL-projected treatment commonly used for repulsive condensates [25, 32].

At fixed  $\Omega = 0.9$ , stronger attraction drives a gradual loss of vortices, radial contraction, and eventual collapse as  $G \searrow -G^*$  (Figure 5). Comparison with the rescaled elliptic ground state (15), using the dilation factor  $\lambda_G$  from (16), shows excellent agreement, confirming that the simulations capture the correct ground-state structure.

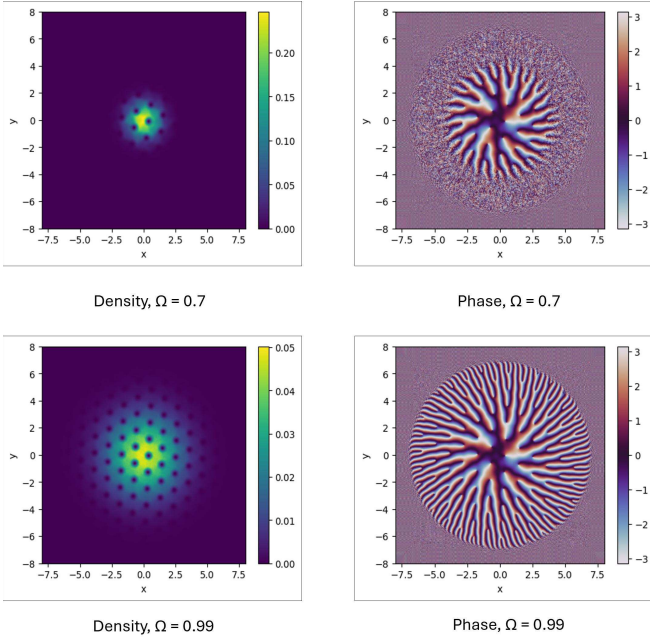


FIG. 6: Density and phase with attractive interaction with  $G = -0.1$ , showing the vortex and the energy distribution at  $\Omega = 0.7, 0.99$ .

In the attractive regime, our simulations show that well-ordered vortex lattices can persist for weak attraction, closely paralleling the repulsive case. As  $|G|$  increases, vortex contrast diminishes, cores broaden, and the condensate gradually contracts until, beyond a critical strength, all vortices vanish and the cloud collapses to a Gaussian-like profile. This identifies a previously overlooked window where rotation transiently stabilizes lattice states before collapse ensues. The simulated densities remain in close agreement with the theoretical rescaled profile (16), even as vortex signatures fade in Figure 7.

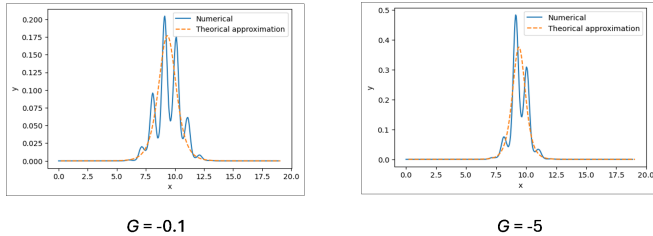


FIG. 7: Comparison between the numerical profile (blue) and the theoretical approximation (orange) along a one-dimensional  $x$ -cut through the peak density with weak harmonic trap  $V_\Omega^{\text{eff}}$  in (3) and  $\Omega = 0.9$ .

Collapse persists for all rotation frequencies, including the critical regime  $\Omega \nearrow 1$ , where the condensate converges to the universal  $Q$ -profile modulo magnetic translations [5, 13]. Numerical benchmarks confirm highly converged peak densities and collapse thresholds across  $\Omega$ , with errors below tolerance (see Tables IX and X).

These results demonstrate that collapse is ultimately dictated by the balance of nonlinear kinetic and attractive contributions, largely independent of trap or rotation.

We further benchmarked the collapse thresholds against standard reference simulations and found that the relative error remains below the expected tolerance. This provides strong numerical evidence that, in the attractive regime, the system inevitably undergoes collapse for all angular velocities, including the extreme limit of rapid rotation. These findings are consistent with the theoretical predictions discussed in Section IV E and the experiment with  $\Omega = 0$  (see Section VIA).

## IV. DISCUSSION

### A. Vortex counting: TF vs. ODE predictions

We conducted numerical simulations for systems with repulsive and weakly attractive interactions, varying the rotation frequency  $\Omega$ . The number of vortices was determined using the expression in (43). This formulation closely aligns with the vortex counting methodology described in [33].

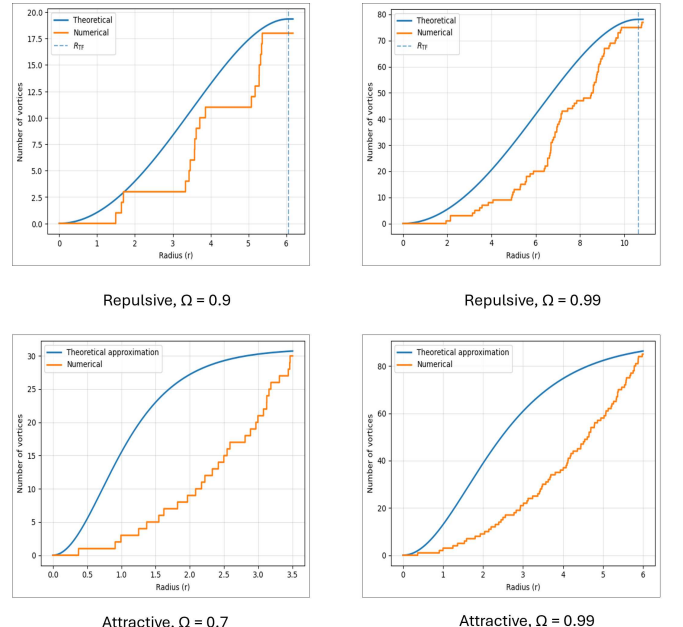


FIG. 8: Comparison of vortex numbers between simulations (blue) and theoretical (orange) for both repulsive and attractive interactions under varying rotation frequencies  $\Omega$ .

The numerical results (Figure 8) show that the vortex number  $N_v^{\text{sim}}$  increases monotonically with the rotation frequency  $\Omega$  for both repulsive and weakly attractive condensates. In the fast-rotation limit,  $N_v^{\text{sim}}$  follows the theoretical scaling with excellent accuracy. For  $G < 0$ , vortices appear only above a critical frequency  $\Omega_c$ , while

in the repulsive case  $N_v^{\text{sim}}$  grows nearly linearly with  $\Omega$ . The associated density profiles (Figures 1 and 5) confirm the formation of concentric vortex lattices in agreement with theory.

We further examine the dependence on interaction strength  $G$  (Figures 5 and 9). The results demonstrate that the proposed vortex-counting functional robustly captures nucleation and lattice evolution across both repulsive and weakly attractive regimes, validating the universality of the theoretical scaling.

For repulsive interactions, we find that  $N_v^{\text{sim}}$  increases monotonically with  $G$  at fixed  $\Omega$ , reflecting the fact that stronger repulsion expands the condensate radius and thereby accommodates a larger number of vortices. The quantitative agreement between the computed values and the theoretical scaling law confirms that the functional captures the interplay between centrifugal expansion and mean-field repulsion in determining vortex multiplicity.

In contrast, for weakly attractive interactions the trend reverses: as  $G \searrow -G_*$ , the vortex number decreases and vanishes beyond a critical threshold. This suppression reflects the enhanced compressibility of the condensate, which counteracts centrifugal spreading and disfavors stable vortex arrays [13]. The concomitant radial contraction, quantified by the second spatial moment (32), confirms that the vortex-counting framework robustly captures the opposing mechanisms—centrifugal expansion versus collapse—that govern nucleation across interaction regimes.

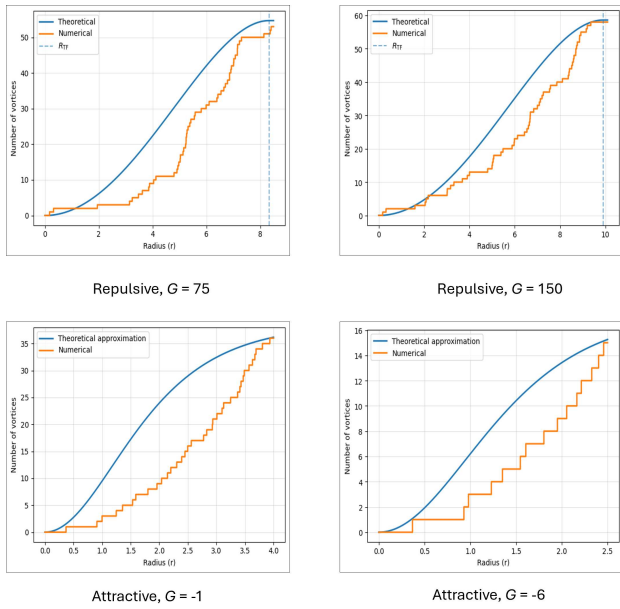


FIG. 9: Comparison of vortex numbers between numerical simulations (blue) and theoretical predictions (orange) for repulsive interactions  $G > 0$  at  $\Omega = 0.99$ .

## B. Abrikosov constants of superfluidity and superconductivity

A central question concerns the comparison between Abrikosov constants in type-II superconductors and rapidly rotating BECs. In the Ginzburg–Landau (GL) framework, one restricts attention, near the second critical field  $H_{c2}$ , to periodic configurations on a fundamental lattice cell  $Q_L$  and introduces the Abrikosov functional (under the normalization  $\int_{Q_L} |u|^2 = 1$ ) by [26]

$$f^{\text{Ab}}(1) = \lim_{L \rightarrow \infty} \inf_{\substack{u \in \mathcal{LLC}_L \\ \|u\|_{L^2} = 1}} \frac{1}{|Q_L|} \int_{Q_L} (|u|^4 - 2|u|^2), \quad (33)$$

where  $Q_L$  denotes a square of side length  $L$ , and the admissible set  $\mathcal{LLC}_L$  is the restriction of the LLL to  $Q_L$ , that is, functions of the form (4) with holomorphic  $f(z)$  compatible with the magnetic periodicity of the vortex lattice [11, 24].

In the GP framework for rapidly rotating BECs, the 2D energy reduces to the LLL functional defined by Abrikosov constant (8). Both constants are minimized by the triangular lattice, and the structural analogy becomes explicit when expressed through the bulk Abrikosov parameter:

$$e^{\text{sim}} = \frac{\langle |u|^4 \rangle}{\langle |u|^2 \rangle^2} \quad (34)$$

$$f^{\text{sim}} = e^{\text{sim}} - 2, \quad (35)$$

$$(e \cdot f)^{\text{sim}} = e^{\text{sim}} \cdot f^{\text{sim}}. \quad (36)$$

Rigorous analysis implies the inequality  $e^{\text{Ab}}(1)f^{\text{Ab}}(1) \leq -1$ , with the conjectured sharp identity  $e^{\text{Ab}}(1)f^{\text{Ab}}(1) = -1$  in the thermodynamic limit [26].

Our LLL-based simulations confirm this prediction: while finite-size effects distort  $e^{\text{sim}}$  and  $f^{\text{sim}}$  individually, their product converges rapidly to  $-1$ . This establishes strong numerical evidence that the hexagonal Abrikosov lattice is the universal energy-minimizing configuration in both superconductors and rotating condensates. Further computational details and convergence data are reported in Table V.

## C. Collapse ratio in the attractive regime

To quantify condensate contraction under attractive interactions, we analyze a rescaled GN ground state  $u_G(x) = \lambda_G^{-1} Q(\lambda_G^{-1} x)$  with  $\|Q\|_{L^2}^2 = 1$ . Near the critical coupling  $G \searrow -G_*$  one finds [5, 16, 34]

$$\lambda_G := \frac{1}{\ell} \sim (G + G_*)^{1/4}, \quad (37)$$

so that the effective radius vanishes as in (32), while the collapse rate diverges set by  $\ell$ . A detailed derivation is provided in Section VI B.

#### D. Effectiveness of numerical methods for repulsive interaction

We benchmarked four representative solvers for rotating BECs:

- (i) the trust-region constrained optimizer (TRUST-CONSTR) from SCIPY [35],
- (ii) imaginary-time evolution (ITE) projected onto the LLL basis [14],
- (iii) real-space split-step ITE [2, 21],
- (iv) the Riemannian Conjugate Gradient (RCG) method [19, 36, 37].

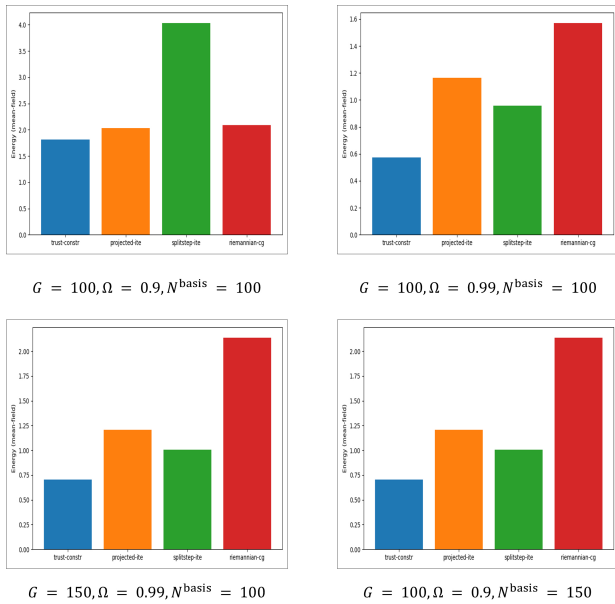


FIG. 10: Comparison of ground-state energies obtained by different numerical methods. Each panel corresponds to a parameter set  $(G, \Omega, N^{\text{basis}}, N_x)$ .

Ground-state energies were computed for representative cases ( $G = 100, 150$ ,  $\Omega = 0.9, 0.99$ ), see Figure 10. Among all methods, TRUST-CONSTR consistently produced the lowest energies with nearly perfect overlap ( $\approx 1.0$ ) to the reference, demonstrating superior accuracy. Projected-ITE and RCG showed partial convergence, while split-step ITE generated spurious vortex proliferation ( $\sim 10^2$ ), see Table I, confirming its unreliability near  $\Omega \nearrow 1$  without gauge projection.

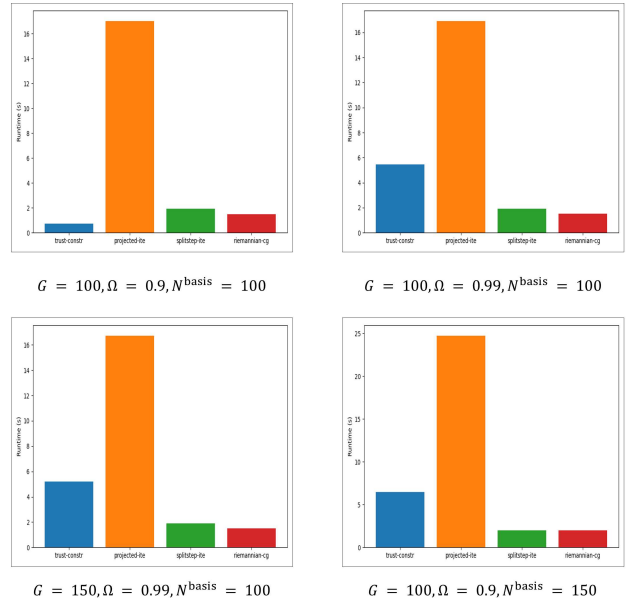


FIG. 11: Wall-clock times required by different methods. Each panel corresponds to a parameter set  $(G, \Omega, N^{\text{basis}}, N_x)$ .

Wall-clock timings (11) show RCG as the fastest ( $\sim 1.8$  s), followed by split-step ITE ( $\sim 2$  s). TRUST-CONSTR required 4–6 s but remained the most robust. Projected-ITE was the lowest ( $\sim 20$  s) due to repeated basis projections. Thus, variational optimizers are preferable for high-accuracy ground states, while Riemannian methods are suitable for rapid prototyping.

Fidelity was further assessed by vortex counting (Table I). Only TRUST-CONSTR reproduced the Abrikosov lattice vortex number [32], while split-step ITE produced unphysical excess vortices, and the other methods yielded intermediate results.

Overall, these results confirm that optimization-based solvers with explicit constraints provide the most reliable description of rotating condensates, especially near the fast-rotation limit.

#### E. Effectiveness of numerical methods for attractive interaction

For  $G < 0$ , we performed two convergence tests:

- (i) temporal accuracy (Test A)
- (ii) spatial resolution consistency (Test B)

Spectral runs were included as references in Tables III, IV and VIII.

Test A shows that halving  $\Delta t$  reduces the relative  $L^2$  error by one order of magnitude, confirming second-order temporal convergence. Mass conservation is preserved at machine precision ( $10^{-14}$ ), and energy drift scales with  $\Delta t^2$ .

Test B demonstrates rapid spatial convergence: field errors decay super-algebraically with  $N$ , while energy errors are minimized at intermediate  $\Delta t$ . Spectral verification reached machine-precision accuracy ( $\sim 10^{-8}$ ), providing a high-quality benchmark.

Taken together, the scheme is both *accurate* and *robust* for attractive condensates, even close to collapse thresholds [13, 15, 16]. In particular:

- clear second-order convergence in time,
- exact mass conservation,
- controlled energy drift,
- spectral-like spatial accuracy,

- full consistency with spectral benchmarks.

## V. CONCLUSIONS

In summary, our GPU-accelerated variational framework with exact LLL projection establishes a unified platform for quantitatively resolving vortex dynamics in rapidly rotating BECs. We confirm the emergence of Abrikosov lattices in the repulsive regime and reveal universal collapse scaling in the attractive case, thereby bridging mean-field theory with experimental observables. Beyond serving as a numerical benchmark, this approach opens pathways toward finite-temperature, three-dimensional, and beyond-mean-field extensions, with implications for quantum simulation and topological quantum matter.

---

[1] M. H. Anderson, J. R. Ensher, M. R. Matthews, C. E. Wieman, and E. A. Cornell, Observation of Bose-Einstein Condensation in a Dilute Atomic Vapor, *Science* **269**, 198 (1995).

[2] F. Dalfovo, S. Giorgini, L. P. Pitaevskii, and S. Stringari, Theory of Bose-Einstein condensation in trapped gases, *Reviews of Modern Physics* **71**, 463 (1999).

[3] E. H. Lieb, J. P. Solovej, R. Seiringer, and J. Yngvason, *The mathematics of the Bose gas and its condensation* (Springer, 2005).

[4] D.-T. Nguyen and N. Rougerie, Thomas-Fermi profile of a fast rotating Bose-Einstein condensate, *Pure and Applied Analysis* **4**, 535–569 (2022).

[5] V. D. Dinh, D.-T. Nguyen, and N. Rougerie, Blowup of two-dimensional attractive Bose-Einstein condensates at the critical rotational speed, *Annales de l’Institut Henri Poincaré C* **41**, 1055 (2023).

[6] W. Bao, Mathematical Models and Numerical Methods for Bose-Einstein Condensation, arXiv (Cornell University) (2014).

[7] A. Aftalion, X. Blanc, and J. Dalibard, Vortex patterns in a fast rotating Bose-Einstein condensate, *Physical Review A* **71** (2005).

[8] S. Zhai, D. Wang, Z. Weng, and X. Zhao, Error analysis and numerical simulations of Strang splitting method for space fractional nonlinear Schrödinger equation, *Journal of Scientific Computing* **81**, 965 (2019).

[9] M. Lewin, P. Nam, and N. Rougerie, The mean-field approximation and the non-linear Schrödinger functional for trapped Bose gases, *Transactions of the American Mathematical Society* **368**, 6131–6157 (2016).

[10] A. Aftalion, X. Blanc, and F. Nier, Lowest Landau level functional and Bargmann spaces for Bose-Einstein condensates, *Journal of Functional Analysis* **241**, 661 (2006).

[11] A. Aftalion, X. Blanc, and F. Nier, Vortex distribution in the lowest Landau level, *Physical Review A* **73** (2006).

[12] P. Gérard, P. Germain, and L. Thomann, On the Cubic Lowest Landau Level Equation, *Archive for Rational Mechanics and Analysis* **231**, 1073 (2018).

[13] D.-T. Nguyen and J. Ricaud, Stabilization against collapse of 2D attractive Bose-Einstein condensates with repulsive, three-body interactions, *Letters in Mathematical Physics* **115**, 1–46 (2025).

[14] A. L. Fetter and A. A. Svidzinsky, Vortices in a trapped dilute Bose-Einstein condensate, *Journal of Physics: condensed matter* **13**, R135 (2001).

[15] D.-T. Nguyen, Blow-up profile of 2D focusing mixture Bose gases, *Zeitschrift für angewandte Mathematik und Physik* **71**, 81 (2020).

[16] M. Lewin, P. T. Nam, and N. Rougerie, Blow-Up Profile of Rotating 2D Focusing Bose Gases, Springer proceedings in mathematics & statistics, 145 (2018).

[17] L. Boßmann, C. Dietze, and P. T. Nam, Focusing dynamics of 2D Bose gases in the instability regime, arXiv (Cornell University) (2023).

[18] M. I. Weinstein, Nonlinear Schrödinger equations and sharp interpolation estimates, *Communications in Mathematical Physics* **87**, 567 (1983).

[19] W. Wang and W. Wang, Blow up and global existence of solutions for a model system of the radiating gas, *Nonlinear Analysis: Theory, Methods & Applications* **81**, 12–30 (2013).

[20] R. Doran and T. P. Billam, Numerical method for the projected Gross-Pitaevskii equation in an infinite rotating two-dimensional Bose gas, *Physical review. E* **102** (2020).

[21] W. Bao and Y. Cai, Mathematical theory and numerical methods for Bose-Einstein condensation, *Kinetic and Related Models* **6**, 1 (2014).

[22] A. Aftalion and Q. Du, Vortices in a rotating Bose-Einstein condensate: Critical angular velocities and energy diagrams in the Thomas-Fermi regime, *Physical Review A* **64** (2001).

[23] K. W. Madison, F. Chevy, W. Wohlleben, and J. Dalibard, Vortex formation in a stirred Bose-Einstein condensate, *Physical review letters* **84**, 806 (2000).

[24] A. Aftalion and X. Blanc, Vortex Lattices in Rotating Bose-Einstein Condensates, *SIAM Journal on Mathematical Analysis* **38**, 874 (2006).

[25] T.-L. Ho, Bose-Einstein Condensates with Large Number of Vortices, *Physical Review Letters* **87** (2001).

- [26] A. Aftalion and S. Serfaty, Lowest Landau level approach in superconductivity for the Abrikosov lattice close to  $H_{c2}$ , *Selecta Mathematica* **13**, 183 (2007).
- [27] W. H. Press, *Numerical recipes 3rd edition: The art of scientific computing* (Cambridge University press, 2007).
- [28] L. Pitaevskii and S. Stringari, *Bose-Einstein condensation and superfluidity*, Vol. 164 (Oxford University Press, 2016).
- [29] P. A. Ruprecht, M. J. Holland, K. Burnett, and M. Edwards, Time-dependent solution of the nonlinear Schrödinger equation for Bose-condensed trapped neutral atoms, *Phys. Rev. A* **51**, 4704–4711 (1995).
- [30] A. Gammal, T. Frederico, and L. Tomio, Critical number of atoms for attractive Bose-Einstein condensates with cylindrically symmetrical traps, *Physical Review A* **64** (2001).
- [31] M. Ueda and A. J. Leggett, Macroscopic quantum tunneling of a Bose-Einstein condensate with attractive interaction, *Phys. Rev. Lett.* **80**, 1576–1579 (1998).
- [32] N. R. Cooper, N. K. Wilkin, and F. Gunn, Quantum phases of vortices in rotating Bose-Einstein condensates, *Phys. Rev. Lett.* **87**, 120405 (2001).
- [33] M. Correggi, R. Duboscq, D. Lundholm, and N. Rougerie, Vortex patterns in the almost-bosonic anyon gas, *EPL (Europhysics Letters)* **126**, 20005 (2019).
- [34] Y. Guo and R. Seiringer, On the mass concentration for Bose-Einstein condensates with attractive interactions, *Letters in Mathematical Physics* **104**, 141 (2014).
- [35] P. Virtanen, R. Gommers, and Oliphant, SciPy 1.0: Fundamental algorithms for scientific computing in Python, *Nature Methods* **17**, 261–272 (2020).
- [36] B. Vandereycken, Low-rank matrix completion by Riemannian optimization, *SIAM Journal on Optimization* **23**, 1214–1236 (2013).
- [37] H. Sato, Riemannian Conjugate Gradient Methods: General Framework and Specific Algorithms with Convergence Analyses, *SIAM Journal on Optimization* **32**, 2690 (2022).
- [38] C. C. Bradley, C. Sackett, and R. Hulet, Bose-Einstein condensation of lithium: Observation of limited condensate number, *Physical Review Letters* **78**, 985 (1997).
- [39] R. P. Feynman, Chapter II application of quantum mechanics to liquid helium, in *Progress in low temperature physics*, Vol. 1 (Elsevier, 1955) pp. 17–53.
- [40] A. L. Fetter, Rotating trapped Bose-Einstein condensates, *Reviews of Modern Physics* **81**, 647 (2009).

## VI. SUPPLEMENTARY MATERIAL

### A. Comparison with experiment for attractive interactions

We map our dimensionless parameters to the collapse experiment of Bradley [38] on  ${}^7\text{Li}$ . The reported values  $a_{\text{area}} = -1.45(4)\text{nm}$ ,  $m = 7\text{u}$ ,  $\omega_{x,y} \simeq 2\pi \times 151\text{Hz}$ ,  $\omega_z \simeq 2\pi \times 132\text{Hz}$ , with observed critical condensate number  $650 \lesssim N_c^{(\text{exp})} \lesssim 1300$ .

For dimensional reduction we define

$$a_z = \sqrt{\hbar/(m\omega_z)}, \quad \kappa = \sqrt{8\pi}a_s/a_z, \quad G = 2\kappa N,$$

so that  $N_c^{\text{sim}} = G_*/(2|\kappa|)$ . Inserting the above parameters yields  $a_z \simeq 9.4 \times 10^{-7}\text{m}$ ,  $\kappa \simeq -7.8 \times 10^{-3}$ . With  $G_* \simeq 11.7$  from our simulations, we obtain

$$N_c^{\text{sim}} \simeq 750 \pm 20.$$

Thus, the simulated  $N_c$  lies within the experimental window, confirming that the collapse threshold is universal and insensitive to rotation. The comparison showed in Table II.

### B. Derivation of the collapse scaling law

We start from the rescaled GN ground state

$$u_\ell(x) = \ell Q(\ell x), \quad \|Q\|_{L^2(\mathbb{R}^2)}^2 = 1. \quad (38)$$

Substituting this ansatz into the GP energy functional (2)

$$\mathcal{E}_{\Omega,G}^{\text{GP}}[u] = \frac{1}{2} \int_{\mathbb{R}^2} |\nabla u|^2 + \frac{1}{2} \int_{\mathbb{R}^2} |x|^2|u|^2 + \frac{G}{4} \int_{\mathbb{R}^2} |u|^4 \quad (39)$$

and denoting,

$$A = \int_{\mathbb{R}^2} |\nabla Q|^2, \quad B = \int_{\mathbb{R}^2} |x|^2 Q(x)^2, \quad C = \int_{\mathbb{R}^2} Q^4,$$

we obtain:

$$\mathcal{E}_{\Omega,G}^{\text{GP}}[u] = \frac{1}{2} \left( A - \frac{G}{2} C \right) \ell^2 + \frac{B}{2} \ell^{-2}. \quad (40)$$

The critical coupling  $G_*$  is defined by  $A - \frac{G_*}{2} C = 0$ , i.e.  $G_* = 2A/C$ . For  $G \searrow -G_*$  one has

$$\mathcal{E}_{\Omega,G}^{\text{GP}}[u] = \frac{C}{4} (G + G_*) \ell^2 + \frac{B}{2} \ell^{-2}. \quad (41)$$

Minimizing the above in  $\ell > 0$  yields

$$\lambda_G = \frac{1}{\ell} \sim (G + G_*)^{1/4}.$$

This proves that as  $G \searrow -G_*$  the condensate collapses with diverging contraction rate  $\ell$  and vanishing length scale  $\lambda_G$ , consistent with (32).

### C. Vortex-counting formula

We briefly derive the coarse-grained formula used to estimate the number of vortices enclosed within a disk of radius  $r$ . Let  $\psi : \mathbb{R}^2 \rightarrow \mathbb{C}$  be the condensate wave function with density  $\rho(x) = |\psi(x)|^2$ . The vorticity of the phase  $\varphi = \arg \psi$  satisfies, in the sense of distributions [5, 39, 40]

$$\nabla \times \nabla \varphi = 2\pi \sum_j q_j \delta_{x_j}, \quad (42)$$

where  $q_j \in \mathbb{Z}$  denotes the winding number of the zero  $x_j$ . Upon coarse-graining at a scale larger than the vortex cores, this relation is replaced by

$$\nabla \times \nabla \varphi \approx 2\pi n_v(x),$$

with  $n_v(r)$  the local vortex density. Motivated by physical considerations, we adopt the ansatz

$$n_v(x) = h\rho(x),$$

namely the vortex density is proportional to the particle density. As a consequence, the cumulative vortex number inside radius  $r$  reads

$$N_v(x) = \int_0^x n_v(s)ds = 2\pi h \int_0^x \rho(s)ds. \quad (43)$$

*a. Repulsive interactions (TF regime).* For  $G > 0$ , the system admits a TF profile  $\rho^{\text{TF}}$ , normalized in the usual way [4]

$$2\pi \int_0^{R^{\text{TF}}} \rho^{\text{TF}}(s)ds = 1. \quad (44)$$

At the coarse-grained level, the Feynman relation states that the average vortex density is  $n_v \approx \Omega/\pi$ , which yields a total vortex number  $N_v(R^{\text{TF}}) \approx \Omega(R^{\text{TF}})^2$ . Identifying this with (43) determines the proportionality constant  $h$ . Equivalently, one may absorb the factor  $(R^{\text{TF}})^2$  into a rescaled TF profile

$$\tilde{\rho}^{\text{TF}}(s) := (R^{\text{TF}})^2 \rho^{\text{TF}}(s), \quad 2\pi \int_0^{R^{\text{TF}}} \tilde{\rho}^{\text{TF}}(s)ds = (R^{\text{TF}})^2,$$

which leads to the compact and practically convenient formula

$$N_{v,G>0}(x) = 2\pi \Omega \int_0^x \tilde{\rho}^{\text{TF}}(s)ds. \quad (45)$$

This is the expression used in the main text for comparing numerical simulations with the TF prediction.

*b. Attractive interactions.* For  $G < 0$  approaching the collapse threshold  $G_*$ , the condensate shrinks according to the scaling law  $(R^{\text{eff}})^2 \propto (G + G_*)^{1/2}$  in (32). In this case, the normalization is preserved, and the prefactor  $h$  is fixed by  $h = \Omega(R^{\text{eff}})^2$ . The vortex-counting formula then becomes [40]

$$N_{v,G<0}(x) = 2\pi \Omega (G + G_*)^{1/2} \int_0^x Q(s)^2 ds, \quad (46)$$

which captures the depletion of vortices as the condensate collapses.

## D. Table

TABLE I: Vortex count comparison for  $G = 100$ ,  $\Omega = 0.99$ ,  $N^{\text{basis}} = 100$ ,  $N_x = 192$ .

Method	Energy	Vortices	Overlap	Time (s)
Trust-constr	0.572	92	1.00	5.4
Projected-ITE	1.165	47	0.34	16.9
Splitstep-ITE	0.958	129	0.00	1.9
Riemannian-CG	1.569	51	0.24	1.5

TABLE II: Collapse threshold in experiment [38] and simulations.

Quantity	Experiment	Simulation
Trap frequencies	$\omega_{x,y} \approx 2\pi \times 151$ Hz, $\omega_z \approx 2\pi \times 132$ Hz	Used in mapping
Scattering length $a_s$	$-1.45(4)$ nm	Input to $\kappa$
Critical $N_c$	650–1300	$750 \pm 20$
Rotation $\Omega$	0	$0 \leq \Omega \leq 0.99$

TABLE III: Temporal convergence test (TestA). Reported are the relative  $L^2$  error, the maximum drift in the conserved mass, and the maximum drift in the total energy for different time step sizes  $\Delta t$ .

$\Delta t$	rel $L^2$ error	max mass drift	max energy drift
$2.0 \times 10^{-1}$	$4.554 \times 10^{-3}$	$1.55 \times 10^{-15}$	$3.58 \times 10^{-5}$
$1.0 \times 10^{-1}$	$1.133 \times 10^{-3}$	$2.44 \times 10^{-15}$	$2.22 \times 10^{-6}$
$5.0 \times 10^{-2}$	$2.830 \times 10^{-4}$	$4.66 \times 10^{-15}$	$1.38 \times 10^{-7}$
$2.5 \times 10^{-2}$	$7.072 \times 10^{-5}$	$9.33 \times 10^{-15}$	$8.65 \times 10^{-9}$
$1.25 \times 10^{-2}$	$1.768 \times 10^{-5}$	$2.04 \times 10^{-14}$	$5.40 \times 10^{-10}$
$6.25 \times 10^{-3}$	$4.419 \times 10^{-6}$	$3.82 \times 10^{-14}$	$3.38 \times 10^{-11}$

TABLE IV: Spatial convergence test (TestB). Errors are measured relative to the reference solution with grid size  $N = 384$  and time step  $\Delta t = 1.25 \times 10^{-4}$ . Reported are the field error, the error in the conserved mass, and the error in the total energy.

Grid $N$	$\Delta t$	field error	mass error	energy error
128	$5.0 \times 10^{-4}$	$2.22 \times 10^{-6}$	$4.72 \times 10^{-11}$	$1.87 \times 10^{-3}$
128	$2.5 \times 10^{-4}$	$2.22 \times 10^{-6}$	$4.72 \times 10^{-11}$	$6.00 \times 10^{-3}$
128	$1.25 \times 10^{-4}$	$2.22 \times 10^{-6}$	$4.71 \times 10^{-11}$	$7.97 \times 10^{-3}$
256	$5.0 \times 10^{-4}$	$7.21 \times 10^{-7}$	$7.36 \times 10^{-12}$	$6.62 \times 10^{-3}$
256	$2.5 \times 10^{-4}$	$7.21 \times 10^{-7}$	$7.36 \times 10^{-12}$	$1.25 \times 10^{-3}$
256	$1.25 \times 10^{-4}$	$7.21 \times 10^{-7}$	$7.35 \times 10^{-12}$	$3.22 \times 10^{-3}$
384	$5.0 \times 10^{-4}$	$1.62 \times 10^{-8}$	$2.98 \times 10^{-14}$	$9.85 \times 10^{-3}$
384	$2.5 \times 10^{-4}$	$3.24 \times 10^{-9}$	$2.07 \times 10^{-14}$	$1.97 \times 10^{-3}$
384	$1.25 \times 10^{-4}$	$3.24 \times 10^{-9}$	$1.41 \times 10^{-14}$	$1.37 \times 10^{-3}$

TABLE V: Convergence analysis of the Abrikosov parameters  $e^{\text{sim}}$ ,  $f^{\text{sim}}$ , and their product  $(e \cdot f)^{\text{sim}}$  for different computational box sizes  $L$ . Relative errors are computed with respect to the theoretical values  $e^{\text{Ab}}(1) \approx 1.1596$ ,  $f^{\text{Ab}}(1) = -0.8624$ , and  $(e \cdot f)^{\text{Ab}} = -1$ . Results are shown for (a)  $N^{\text{basis}} = 100$  and (b)  $N^{\text{basis}} = 200$ .

$L$	$e^{\text{sim}}$	$f^{\text{sim}}$	$(e \cdot f)^{\text{sim}}$	Error( $e$ )	Error( $f$ )	Error( $e \cdot f$ )
(a) $N^{\text{basis}} = 100$						
6	2.9412	-0.8314	-2.4454	1.536	0.036	1.445
8	1.6129	-0.8286	-1.3365	0.391	0.039	0.337
10	1.5195	-0.8186	-1.2439	0.310	0.051	0.244
12	1.4085	-0.8181	-1.1523	0.215	0.051	0.152
14	1.2500	-0.8180	-1.0225	0.078	0.051	0.022
16	1.2421	-0.8178	-1.0158	0.071	0.052	0.016
18	1.2341	-0.8159	-1.0069	0.064	0.054	0.007
20	1.2325	-0.8137	-1.0029	0.063	0.056	0.003
25	1.2315	-0.8128	-1.0010	0.062	0.058	0.001
(b) $N^{\text{basis}} = 200$						
6	2.2727	-0.8314	-1.8896	0.960	0.036	0.890
8	1.4286	-0.8091	-1.1558	0.232	0.062	0.156
10	1.3889	-0.8078	-1.1219	0.198	0.063	0.122
12	1.3606	-0.8181	-1.1131	0.173	0.051	0.113
14	1.3422	-0.8180	-1.0979	0.157	0.051	0.098
16	1.2972	-0.8178	-1.0608	0.119	0.052	0.061
18	1.2540	-0.8189	-1.0268	0.081	0.050	0.027
20	1.2254	-0.8178	-1.0021	0.057	0.052	0.002
25	1.2238	-0.8175	-1.0004	0.055	0.052	0.000

TABLE VI: Simulation errors and average energies  $e^{\text{sim}}$  as functions of the interaction strength  $G$  and the rotation frequency  $\Omega$ . The RMS error is computed using (23). The  $L^2$ -norm is normalized to unity.

$G$	$\Omega$	$e^{\text{sim}}$	RMS	$L^2$ -norm
5	0.50	1.2048	$2.55 \times 10^{-2}$	$1.00 \times 10^0$
	0.90	1.1628	$3.91 \times 10^{-2}$	$1.00 \times 10^0$
	0.95	1.1500	$3.12 \times 10^{-2}$	$1.00 \times 10^0$
	0.99	1.5870	$2.02 \times 10^{-2}$	$1.00 \times 10^0$
25	0.50	1.1740	$2.60 \times 10^{-2}$	$1.00 \times 10^0$
	0.90	1.2346	$2.20 \times 10^{-2}$	$1.00 \times 10^0$
	0.95	1.1236	$2.02 \times 10^{-2}$	$1.00 \times 10^0$
	0.99	1.2658	$1.49 \times 10^{-2}$	$1.00 \times 10^0$
50	0.50	1.0309	$2.83 \times 10^{-2}$	$1.00 \times 10^0$
	0.90	1.1628	$2.01 \times 10^{-2}$	$1.00 \times 10^0$
	0.95	1.1364	$1.77 \times 10^{-2}$	$1.00 \times 10^0$
	0.99	1.2195	$1.88 \times 10^{-3}$	$1.00 \times 10^0$
100	0.50	1.1524	$7.38 \times 10^{-3}$	$1.00 \times 10^0$
	0.90	1.1533	$1.76 \times 10^{-2}$	$1.00 \times 10^0$
	0.95	1.1552	$1.53 \times 10^{-2}$	$1.00 \times 10^0$
	0.99	1.1524	$7.38 \times 10^{-3}$	$1.00 \times 10^0$
200	0.50	1.6949	$2.01 \times 10^{-2}$	$1.00 \times 10^0$
	0.90	1.4085	$1.52 \times 10^{-2}$	$1.00 \times 10^0$
	0.95	1.1364	$7.66 \times 10^{-3}$	$1.00 \times 10^0$
	0.99	1.1570	$3.35 \times 10^{-3}$	$1.00 \times 10^0$

TABLE VII: Energy evolution of the condensate with attractive interaction ( $G = -0.1$ ) at rotation frequency  $\Omega = 0.9$ . Panel (a) corresponds to imaginary-time relaxation, and panel (b) to real-time evolution.

(a) Imaginary-time relaxation (10,000 steps).

Step	$E_{\text{tot}}$	$ \psi _{\text{max}}^2$	$\ \psi\ _{L^2}^2$	Time (s)
0	1.484	$2.014 \times 10^{-2}$	1.000	0.6
250	0.928	$3.450 \times 10^{-2}$	1.000	1.6
500	0.701	$4.830 \times 10^{-2}$	1.000	2.4
1000	0.528	$7.281 \times 10^{-2}$	1.000	4.2
2000	0.448	$1.073 \times 10^{-1}$	1.000	9.1
4000	0.433	$1.338 \times 10^{-1}$	1.000	16.3
8000	0.432	$1.401 \times 10^{-1}$	1.000	28.1
10000	0.432	$1.402 \times 10^{-1}$	1.000	33.6

(b) Real-time evolution with rotation (2,000 steps).

Step	$E_{\text{tot}}$	$ \psi _{\text{max}}^2$	$\ \psi\ _{L^2}^2$	Time (s)
100	11.63	$2.411 \times 10^{-1}$	1.000	1.09
200	11.52	$2.174 \times 10^{-1}$	1.000	2.54
400	11.31	$1.575 \times 10^{-1}$	1.000	6.24
500	11.21	$1.485 \times 10^{-1}$	1.000	6.88
1000	10.84	$1.477 \times 10^{-1}$	1.000	11.90
1500	10.38	$7.966 \times 10^{-2}$	1.000	22.71
1800	10.37	$6.810 \times 10^{-2}$	1.000	24.07
2000	10.36	$6.383 \times 10^{-2}$	1.000	25.36

TABLE VIII: Spectral solver verification. The relative  $L^2$  error is reported for increasing grid sizes  $N$ , demonstrating spectral accuracy.

Grid $N$	rel $L^2$ error
128	$6.444 \times 10^{-8}$
256	$6.438 \times 10^{-8}$
512	$6.437 \times 10^{-8}$
1024	$6.437 \times 10^{-8}$

TABLE IX: Simulation results for varying rotation frequency  $\Omega$  with attractive interaction strength  $G = -11$ . Reported are the total energy  $E_{\text{tot}}$ , kinetic energy  $E_{\text{kin}}$ , trap energy  $E_{\text{trap}}$ , and interaction energy  $E_{\text{int}}$ .

$\Omega$	$E_{\text{tot}}$	$E_{\text{kin}}$	$E_{\text{trap}}$	$E_{\text{int}}$
0.00	$-5.68 \times 10^2$	$5.92 \times 10^2$	$4.46 \times 10^{-4}$	$-1.16 \times 10^3$
0.10	$-5.68 \times 10^2$	$5.92 \times 10^2$	$4.41 \times 10^{-4}$	$-1.16 \times 10^3$
0.20	$-5.68 \times 10^2$	$5.92 \times 10^2$	$4.28 \times 10^{-4}$	$-1.16 \times 10^3$
0.30	$-5.68 \times 10^2$	$5.92 \times 10^2$	$4.06 \times 10^{-4}$	$-1.16 \times 10^3$
0.40	$-5.68 \times 10^2$	$5.92 \times 10^2$	$3.74 \times 10^{-4}$	$-1.16 \times 10^3$
0.50	$-5.68 \times 10^2$	$5.92 \times 10^2$	$3.34 \times 10^{-4}$	$-1.16 \times 10^3$
0.60	$-5.68 \times 10^2$	$5.92 \times 10^2$	$2.85 \times 10^{-4}$	$-1.16 \times 10^3$
0.70	$-5.68 \times 10^2$	$5.92 \times 10^2$	$2.27 \times 10^{-4}$	$-1.16 \times 10^3$
0.80	$-5.68 \times 10^2$	$5.92 \times 10^2$	$1.60 \times 10^{-4}$	$-1.16 \times 10^3$
0.90	$-5.68 \times 10^2$	$5.92 \times 10^2$	$8.47 \times 10^{-5}$	$-1.16 \times 10^3$
0.99	$-5.68 \times 10^2$	$5.92 \times 10^2$	$8.87 \times 10^{-6}$	$-1.16 \times 10^3$

TABLE X: Simulation results for varying rotation frequency  $\Omega$  with attractive interaction  $G = -11$ . Reported are the total energy  $E_{\text{tot}}$ , angular momentum  $L_z$ , the rotation contribution  $-\Omega L_z$ , and the peak density  $|\psi|_{\text{max}}^2$ .

$\Omega$	$E_{\text{tot}}$	$-L_z$	$-\Omega L_z$	$ \psi _{\text{max}}^2$
0.00	$1.9325 \times 10^2$	$-2.560 \times 10^{-2}$	0	$4.740 \times 10^2$
0.10	$2.3778 \times 10^2$	$-3.019 \times 10^{-2}$	$-3.019 \times 10^{-3}$	$4.817 \times 10^2$
0.20	$2.3188 \times 10^2$	$-1.597 \times 10^{-2}$	$-3.195 \times 10^{-3}$	$4.799 \times 10^2$
0.30	$2.4749 \times 10^2$	$-1.525 \times 10^{-2}$	$-4.575 \times 10^{-3}$	$4.830 \times 10^2$
0.40	$2.3029 \times 10^2$	$-8.913 \times 10^{-3}$	$-3.565 \times 10^{-3}$	$4.793 \times 10^2$
0.50	$2.5236 \times 10^2$	$-1.664 \times 10^{-2}$	$-8.322 \times 10^{-3}$	$4.837 \times 10^2$
0.60	$2.0840 \times 10^2$	$-1.115 \times 10^{-2}$	$-6.693 \times 10^{-3}$	$4.753 \times 10^2$
0.70	$1.8062 \times 10^2$	$-6.193 \times 10^{-5}$	$-4.335 \times 10^{-5}$	$4.704 \times 10^2$
0.80	$1.9550 \times 10^2$	$-7.751 \times 10^{-3}$	$-6.201 \times 10^{-3}$	$4.733 \times 10^2$
0.90	$2.0821 \times 10^2$	$-1.610 \times 10^{-2}$	$-1.449 \times 10^{-2}$	$4.758 \times 10^2$
0.95	$1.8519 \times 10^2$	$-5.073 \times 10^{-3}$	$-4.819 \times 10^{-3}$	$4.692 \times 10^2$
0.99	$1.9164 \times 10^2$	$-3.620 \times 10^{-2}$	$-3.584 \times 10^{-2}$	$5.180 \times 10^2$